Electron-Muon Ranger:
performance in the MICE Muon Beam

The MICE collaboration[†]

The Muon Ionization Cooling Experiment (MICE) will perform a detailed study of ionization cooling to evaluate the feasibility of the technique. To carry out this program, MICE requires an efficient particle-identification (PID) system to identify muons. The Electron-Muon Ranger (EMR) is a fully-active tracking-calorimeter that forms part of the PID system and tags muons that traverse the cooling channel without decaying. The detector is capable of identifying electrons with an efficiency of 98.6%, providing a purity for the MICE beam that exceeds 99.8%. The EMR also proved to be a powerful tool for the reconstruction of muon momenta in the range 100–280 MeV/c.

1 Introduction

Intense muon sources are required for a future Neutrino Factory or Muon Collider [1, 2]. At production, muons occupy a large phase-space volume (emittance), which makes them difficult to accelerate and store. Therefore, the emittance of the muon beams must be reduced, i.e the muons must be "cooled", to maximise the muon flux delivered to the accelerator. Conventional cooling techniques applied to muon beams [3] would leave too few muons to be accelerated since the muon lifetime is short ($\tau_\mu \sim 2.2\,\mu$s). Simulations indicate that the ionization-cooling effect builds quickly enough to deliver the flux and emittance required by the Neutrino Factory and the Muon Collider [4, 5]. The MICE collaboration will study ionization cooling in detail to demonstrate the feasibility of the technique [6].

Ionization cooling proceeds by passing a beam of muons through a low-Z material [7]. The beam loses energy by ionizing the material, reducing its total momentum. Longitudinal momentum is restored by accelerating cavities. The net effect is to reduce the divergence of the beam and the transverse phase-space the beam occupies. The rate of change of the normalised 2D emittance may be approximated by [8]:

$$\frac{d\varepsilon_N}{ds} \simeq -\frac{\varepsilon_N}{\beta^2 E_\mu}\left|\frac{dE_\mu}{ds}\right| + \frac{\beta_\perp (0.014)^2}{2\beta^3 E_\mu m_\mu X_0}\,; \tag{1}$$

where $\beta = v/c$, E_μ, m_μ are the muon velocity, energy and mass respectively. The rate of change of emittance depends on the properties of the absorber and the beam. Cooling is large when the initial emittance of the beam, ε_N, and stopping power of the absorber, $\langle dE_\mu/ds \rangle$, are large. The effect of heating by multiple Coulomb scattering is reduced if the radiation length of the absorber, X_0, is large and the transverse betatron function, $\beta_\perp$, of the beam at the absorber is small. Optimum cooling is achieved with low-Z absorbers, such as liquid hydrogen or lithium hydride, and with solenoidal beam-focussing.

The muon beams at the front-end of a Neutrino Factory or Muon Collider are expected to be similar, with a large transverse normalised emittance of $\varepsilon_N \approx 12$–$20\,\pi$ mm-rad and a momentum spread of ~ 20 MeV/c. The emittance must be reduced to 2–5 π mm-rad for the Neutrino Factory, with further reduction to 0.008 π mm-rad required for a Muon Collider [9]. The Muon Ionization Cooling Experiment (MICE) [10] collaboration intends to demonstrate the feasibility of an ionization-cooling cell suitable for cooling muon beams at a Neutrino

---

[†]Authors are listed at the end of this paper.

Factory. An accurate measurement of the degree of cooling achieved depends on selecting a pure sample of muons by rejecting their parent particles or decay products. The Electron-Muon Ranger (EMR) [11] is a key component of the particle identification system and its performance in the MICE Muon Beam (MMB) is presented here.

1.1 The Muon Ionization Cooling Experiment

Since energy loss by ionization and multiple Coulomb scattering are momentum dependent, the ionization-cooling effect is momentum dependent. MICE will measure the performance of its cooling cell for muon beams with central momenta in the range 140–240 MeV/c and a momentum spread of ~ 20 MeV/c, as would be the case in a Neutrino Factory. This is achieved using a "super focus-focus" lattice cell [12] which is capable of producing a range of $\beta_\perp$ at the position of the absorber.

A schematic of the MICE Muon Beam (MMB) and the MICE experiment is shown in figure 1 and described in detail in [13, 14]. The MMB operates on the ISIS proton synchrotron [15] at the Rutherford Appleton Laboratory. A titanium target [16] samples the ISIS proton beam, producing pions. The pions are transported by the upstream quadrupoles, Q1–3, and are momentum-selected at the first dipole, D1. The high field present in the Decay Solenoid (DS) increases the pion path-length with the result that the bulk of pion decays occur as the beam passes through the DS. The second dipole, D2, is used to momentum-select a 'muon' beam with high purity or a 'calibration' beam containing a mix of muons, pions and electrons. The resultant beam is transported through two quadrupole triplets, Q4–6 and Q7–9, time-of-flight counters [17], TOF0 and TOF1, and Cherenkov detectors, Ckov [18], to the cooling cell. The beam emittance is inflated as it passes through the variable-thickness brass and tungsten 'diffuser' and is measured in the upstream spectrometer solenoid using a scintillating-fibre tracker. The beam then passes through low-Z absorbers and RF cavities prior to being remeasured in the downstream tracker. Upon exiting the cooling cell the beam is incident upon the final time-of-flight detector, TOF2 [19], a pre-shower detector, KL [18], and the Electron-Muon Ranger, EMR [20].

The particle identification system consists of the TOF0, TOF1 and TOF2, Ckov, KL and EMR detectors, which can conceptually be split in two; TOF0–1 and Ckov identifying particle species prior to the cooling cell and TOF2, KL and EMR identifying species after the cooling cell. In combination with time-of-flight information, the EMR is used to distinguish between muons that have successfully traversed the full cooling cell from those that have decayed en-route. This aids in the measurement of beam transmission through the cooling cell, as well as reducing the uncertainty on the emittance measurement.

2 The Electron-Muon Ranger in the MICE Muon Beam

The primary purpose of the EMR is to distinguish between muons and their decay products, identifying muons that have crossed the entire cooling channel [20]. This allows for the selection of a muon beam with a contamination below 1%. The EMR is a tracking calorimeter, consisting of multiple, orthogonal, layers of triangular scintillating bars arranged in planes. This construction allows several discriminating parameters to be determined that may be used to identify particle species at the EMR.

2.1 EMR construction

Figure 2 shows one plane of the EMR, consisting of 59, tessellated, triangular scintillator bars covering an area of 1.21 m^2. Each plane is rotated through 90° with respect to the previous one, such that a pair of planes defines a horizontal and vertical (x, y) interaction coordinate. Light produced by a particle interaction is collected by
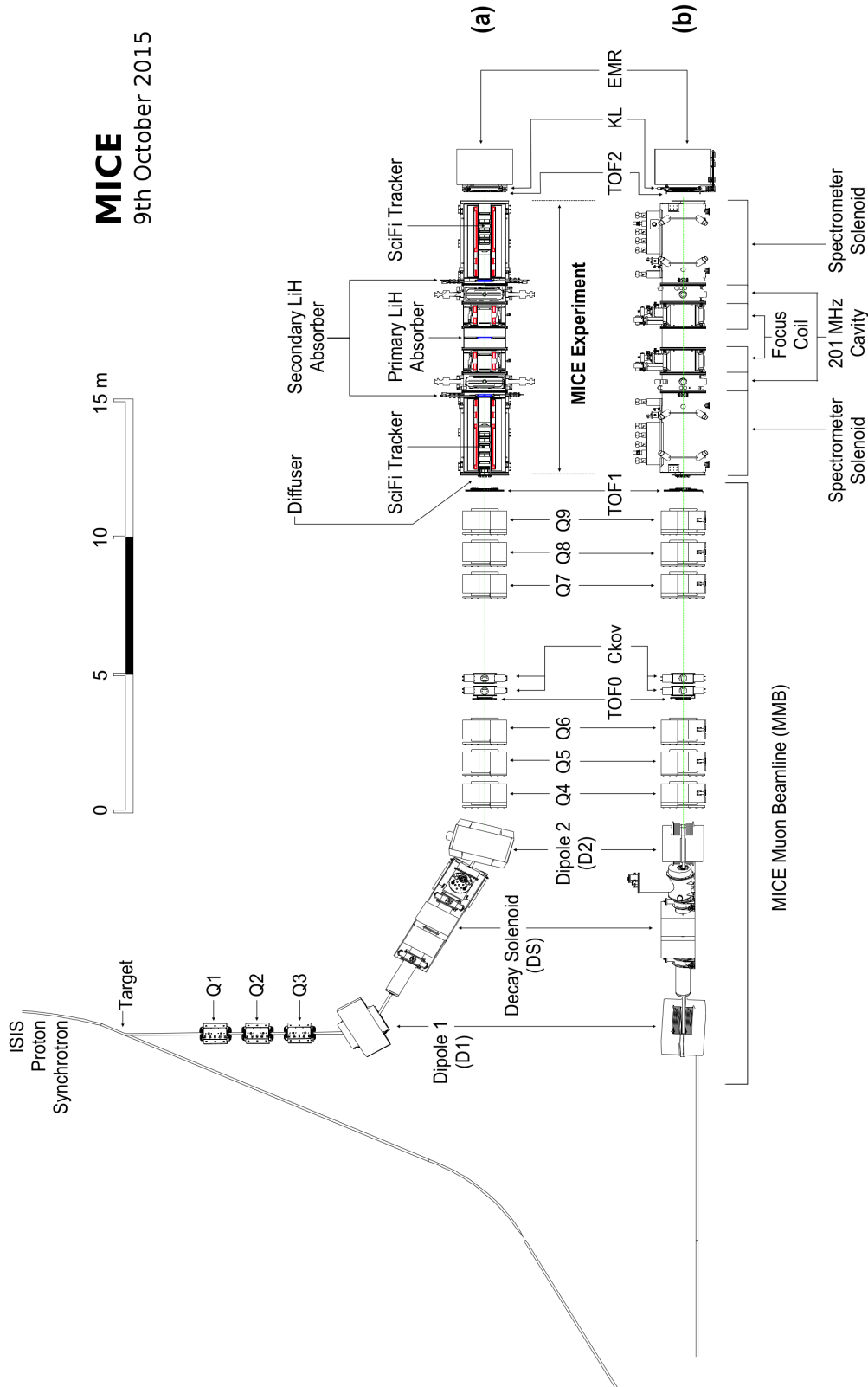
Figure 1: (a) Cross-sectional and (b) side views of the MICE Muon Beam Line (MMB) and the MICE experiment. The Electron-Muon Ranger immediately precedes the beam stop and is the final component of the experiment. The MICE magnet channel (from upstream spectrometer solenoid up to and including the downstream sprectrometer solenoid) was not present when the data reported here was taken.
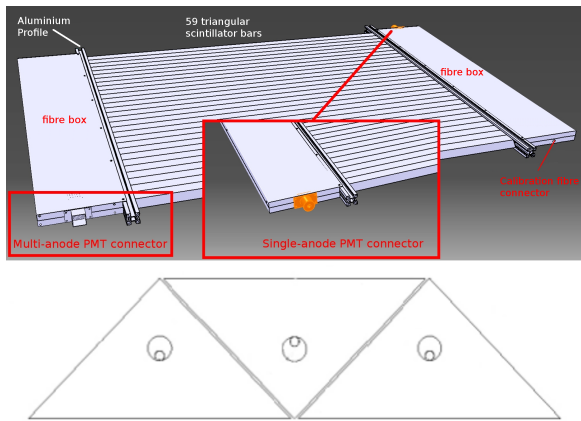
Figure 2: CAD drawing of one EMR plane (top) and cross section of 3 bars and their threaded WLS fibres (bottom).
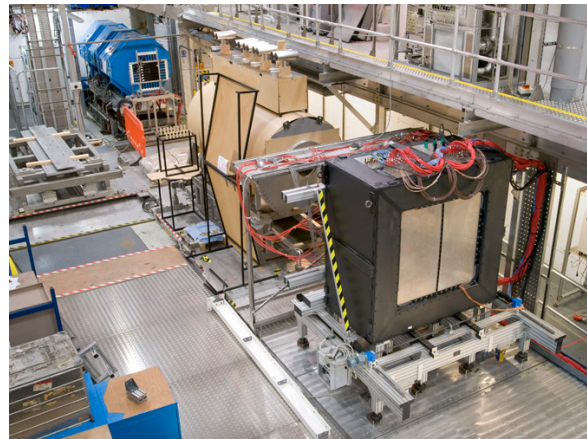

Figure 3: The EMR detector installed in the MICE Hall at the end of the preliminary ('Step I') beam line. The photograph also shows Q7–9 and TOF1 at the top half of the frame. A model of one spectrometer solenoid was positioned in the hall to allow installation procedures to be developed.

the wavelength shifting (WLS) fibre within each bar and is read out at both ends. On one side of the plane, the 59 fibres are bundled together and brought to a conventional single-anode photo-multiplier tube (SAPMT) and on the other side the fibres are individually brought to one of the pixels on a 64-channel multi-anode photo-multiplier tube (MAPMT). A dedicated front-end board reads out and digitizes the MAPMT signals individually by means of fast shapers and discriminators.

Figure 3 shows the full detector, consisting of 48 planes, installed in the MICE Hall at the end of the preliminary ('Step I') beam line [13]. It is enclosed on all sides to ensure a light-tight environment and is magnetically shielded from the cooling cell. A complete description of the design and fabrication of the EMR can be found in [20].

2.2 Data taking

In September 2013, the EMR was placed after TOF2 and KL, $\sim 10\,\mathrm{m}$ from TOF1, and exposed to a variety of beams , prior to the installation of the cooling channel. Both 'muon' and 'calibration' beams over a range of momenta were used to illuminate the detector. These data were used to verify its ability to separate muons from their decay products.

The MMB can be tuned to enhance the production of muons (the 'muon' beam), pions or electrons ('calibration' beams). All beam configurations contain all three particle species, albeit in differing proportions. Beams are defined according to the preferred particle species, e, μ, π and the momentum selected (in the range 100–400 MeV/c) by the D2 magnet, p_{D2}, for the preferred particle type.

Particles travelling from D2 to the EMR cross $\sim 22.7\,\mathrm{m}$ of air as well as the remaining PID detectors (TOFs, Ckov, KL), losing momentum due to ionization. This is expressed as a momentum-loss fraction in figure 4, i.e. the fraction of momentum lost by a particle given its momentum selected at D2. As the EMR must identify muons from electrons over a range of momenta, the beam momentum was scanned from 230–450 MeV/c at D2. This corresponds to 'muon' and 'pion' beam momenta in the range 200–420 MeV/c, with 'electron' beam momentum range of 100–250 MeV/c.
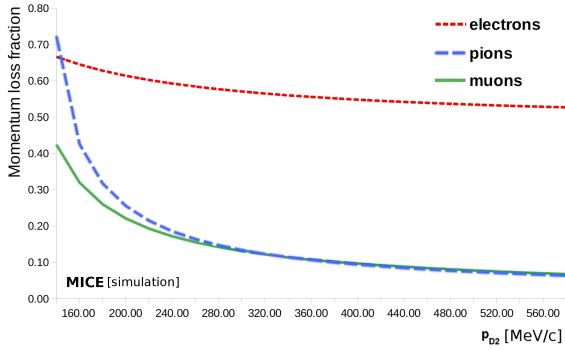
Figure 4: Momentum loss fraction of particles travelling from D2 to the EMR, compared to their momentum at D2 (p_{D2}).
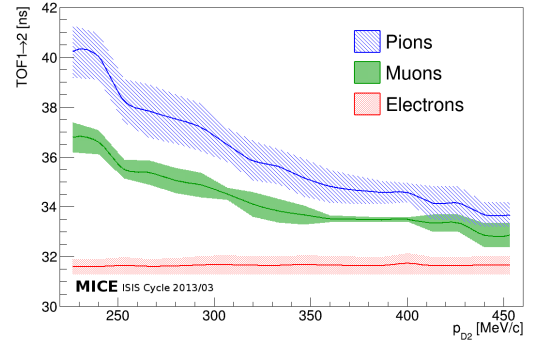

Figure 5: Time-of-flight between the TOF1 and TOF2 detectors (TOF1→2) for a 'calibration' beam selected with an array of momenta at D2 (p_{D2}).

2.3 Particle identification by time-of-flight

The three time-of-flight detectors, TOF0, TOF1 and TOF2, can be used to measure particle momentum, given a particle-species hypothesis. Calibration beams exhibit a three-peak pattern, corresponding to electrons, muons and pions in order of increasing time-of-flight as shown in figure 5 for an array of D2 settings. The time-of-flight for a particular particle is used to define a particle-type hypothesis and to determine the corresponding momentum via $p/E = s/t$, where s is the path length between TOFi and TOFj and $t = t_{TOFi} - t_{TOFj}$.

TOF0 and TOF1 are separated by 7.8 m, whereas TOF1 and TOF2 are separated by 9.4 m. The air between the last two hodoscopes causes a minimum ionizing muon to lose approximately 2 MeV/c, i.e. $\sim 1\%$ of its momentum. The calculation of the probability of a particle being classed as an electron, muon or pion using time-of-flight, for later assessment by the EMR, is based on the assumption that momentum remains approximately constant and that the path length, s, is given by the orthogonal distance between the two TOF planes in question. A combined probability from the three TOFs (i.e. TOF0→1, TOF0→2, TOF1→2) of greater than 90% for a particle to be a muon, leads to that particle being accepted as part of the muon sample, and its momentum to be calculated from its time-of-flight TOF1→2 using the appropriate particle mass. Similarly, a combined probability greater than 90% for a particle to be an electron, leads to that particle being accepted as part of the electron sample. Only the particles that were successfully tagged were used to study the performance of the EMR.

2.4 Momentum loss in TOF2 and the KL

Before entering the EMR, particles pass through the final TOF station, TOF2, and the pre-shower detector, KL. The energy lost by particles in TOF2 is calculated using the Continuous Slowing Down Approximation (CSDA) [21], where the rate of energy loss at every point along its track is assumed to be the same as the total stopping power. TOF2 is composed of two, 2.54 cm thick, planes of polyvinyltoluene (PVT) constituting $0.1 X_0$. On average, minimum ionizing muons lose ~ 10 MeV/c, whereas electrons lose ~ 15 MeV/c as they are ultrarelativistic ($\beta\gamma > 100$) in all cases (figure 6).

The KL is a sampling calorimeter composed of extruded Pb foils and scintillating fibres in a 1 : 2 volume ratio. On average this corresponds to $2.5 X_0$. Electrons shower in the KL before exiting the detector, which makes estimating the energy lost difficult. Muons cross without showering, but still deposit a significant portion
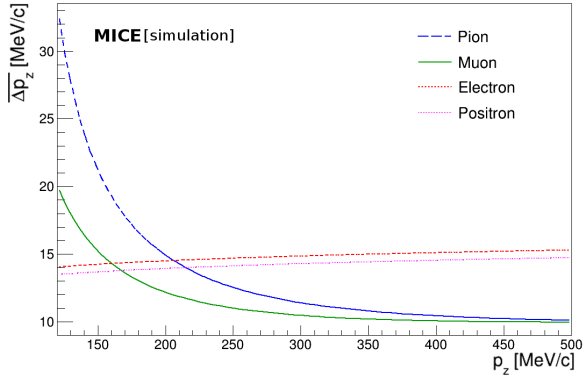
Figure 6: Continuous Slowing Down Approximation of the mean momentum loss ($\overline{\Delta p_z}$) of particles crossing TOF2 with impinging momentum p_z.
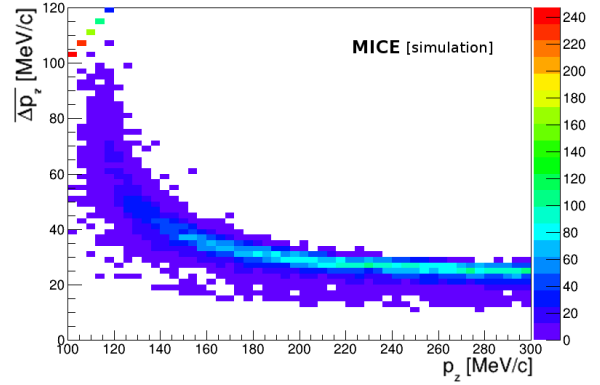

Figure 7: Continuous Slowing Down Approximation of the mean momentum loss ($\overline{\Delta p_z}$) of muons crossing the KL with impinging momentum p_z.

of their energy in the KL. Due to the complexity of the KL detector, a simplified CSDA approximation was developed to estimate momentum loss in the KL (figure 7). Minimum ionizing muons lose, on average, 28 ± 3 MeV/c in the KL.

2.5 Events in the EMR

The EMR is put immediately behind the KL. It is an advantage when using it to identify electron-induced shower since the KL acts as a pre-shower detector.

To characterise the performance of the EMR, particles were first identified with the TOF detectors as described in section 2.3. The particle events included in this analysis consist of a single space-point (X- and Y-view hits) in each TOF and the successful assignment of a particle species. These space points were matched to the relevant EMR hits through their temporal proximity.

The coordinates of a hit are taken to be those of the centre of gravity of the triangular section of the corresponding bar, which is located one third of its height up from its base and bisecting its width. The EMR planes (defined in section 2.1) are placed perpendicular to the beam and their numbering therefore provides the z coordinate. The bar number within that plane determines the second coordinate, q, i.e x is the coordinate provided by the X planes and y the coordinate provided by the Y planes.

An event in the EMR induced by a single positron hitting the KL is represented in the xz and yz projections in figure 8. The positron originates from an 'calibration' beam with a particle momentum of 450 MeV/c selected at D2. The remaining charged particles in the shower create shallow straight tracks in the first half of the detector, while photons produce deep and detached hits that are scattered far into the scintillating volume. Some planes do not record any hit on the particle's path, as might be expected in an electromagnetic shower.

Figure 9 represents the trace left by a single positive muon stopping in the EMR. The impinging muon stops in the 34th plane where the highest energy deposition is recorded (two bars with a time-over-threshold ~ 20 ADC counts[1]). The second part of the track, discriminated from the first part using the timing information, is the positron produced by the muon decay.

---

[1] The time-over-threshold is defined as the width of the low threshold discriminator signal. This signal width, larger for signal with larger amplitudes, depends on the energy lost by the particle. 1 ADC count corresponds to a signal width of 2.5 ns.
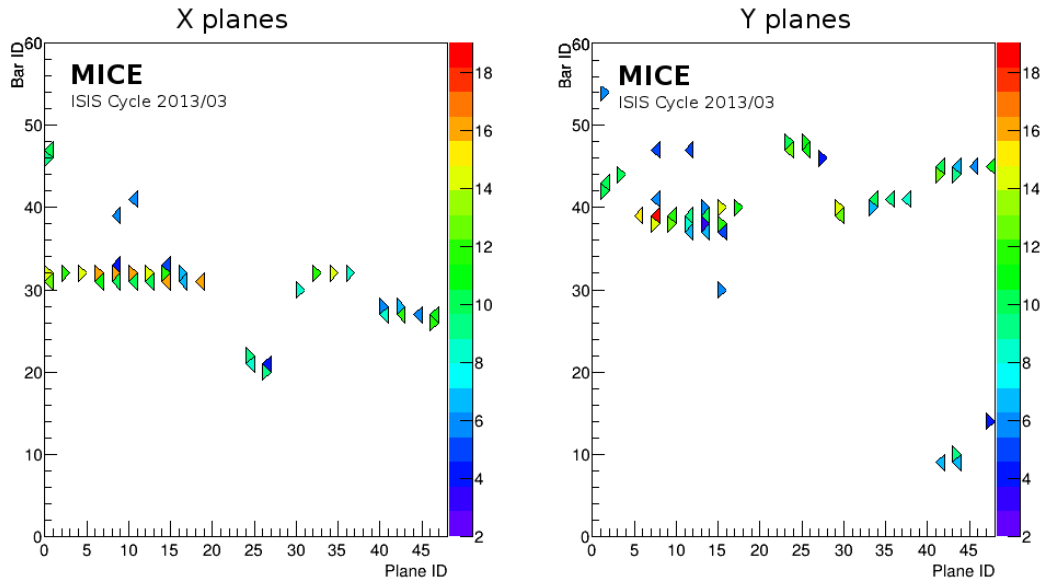
Figure 8: EMR event display of the energy deposited by a positron shower (p_{D2} = 450 MeV/c) in the two projections. The location of a hit is defined by the plane number (Plane ID, 0–47) and bar number (Bar ID, 1–59) and the energy deposited is represented by the colour code in units of time-over-threshold.

Figure 9: EMR event display of the energy deposited by a μ^+ which decays in the detector volume. The location of a hit is defined by the plane number (Plane ID, 0–47) and bar number (Bar ID, 1–59) and the energy deposited is represented by the colour code in units of time-over-threshold.
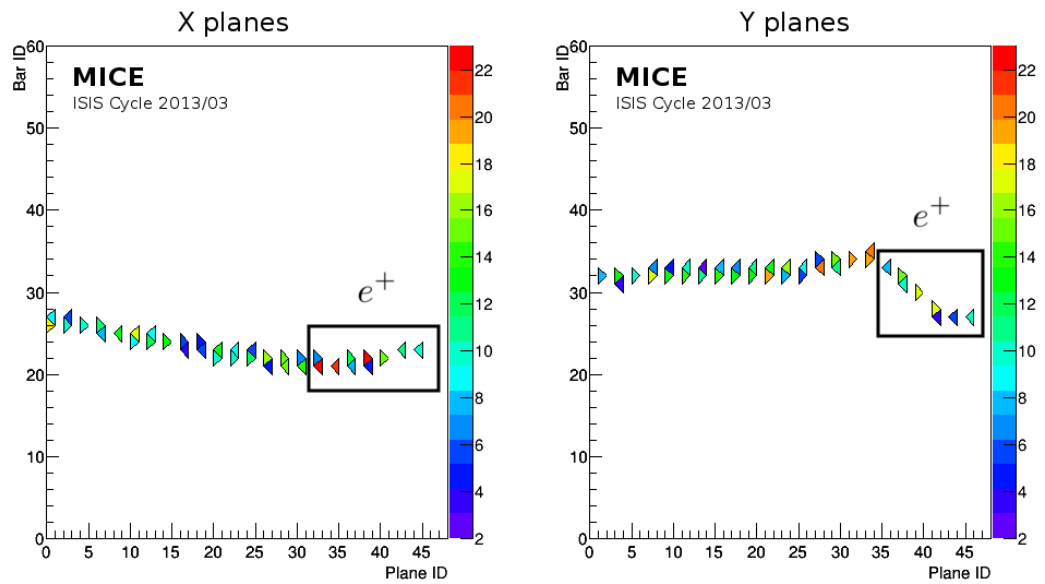
7

3 EMR particle identification variables

Several variables are defined to reduce the information recorded in a complex event to manageable quantities. Due to the different topology of an electron shower and a muon track, a geometrical approach was chosen. Hits from an electromagnetic shower are widely spread throughout the detector, including far downstream into the fiducial volume, without any visible tracks upstream. Muons exhibit clear straight tracks through the EMR before stopping or exiting the volume.

Because of the photon-induced hits at large depth, the range of an electron event is not well defined and thus is not a good variable to use to reject electrons. Non-negligible crosstalk [22] within the multi-anode PMTs prevents the use of a simple shape analysis as muon events could appear wider, thus potentially increasing the loss of real muons. Alternative longitudinal and transverse evaluations of the event are used to distinguish between the two species: the 'plane density' and the 'shower spread', respectively.

3.1 Plane density

This statistic uses the non-continuity of electromagnetic showers to tag electrons and positrons. Electromagnetic showers in the EMR have multiple and disconnected tracks. Planes on the path of the shower are often left without any recorded hit. This characteristic can be contrasted with a muon track that uniformly deposits significant amounts of energy along its path.

Plane density, ρ_P, is defined as the fraction of planes on the path of the particle that record at least one hit. More specifically, it is the average of that density in the two projections, i.e:

$$\rho_P = \frac{N_x + N_y}{Z_x + Z_y} = \frac{N}{Z_x + Z_y} \; ; \tag{2}$$

with N_q the number of planes hit in the qz projection and Z_q the plane number of the most downstream plane in the qz projection, $q = x, y$. N is the total number of planes hit.

The graph in figure 10 shows the plane-density distributions for particles tagged as muons and electrons. Muons have densities close to 1 while electrons have a widely spread distribution centred around $\rho_P \sim 0.5$. It is striking to see how few electron entries overlap the muon cases.

3.2 Shower spread

In this discriminator, only the most energetic hit in each plane, i.e the bar that records the largest time-over-threshold, is kept. This step allows for the rejection of low-energy crosstalk that would dramatically increase the spread of muon tracks. Crosstalk occurs when some of the light carried by a readout fibre leaks onto adjacent channels on the MAPMT, causing artificial hits in bars up to 13 cm away from the actual muon track [22]. Because of the fibre-to-multi-anode PMT mapping, crosstalk only occurs within a single plane, i.e. at a fixed depth in the detector and never between two layers of the calorimeter.

The remaining N_q hits in a given projection are converted into a set of coordinates (z_i, q_i), $i = 1, ..., N_q$ and a line is fitted through these coordinates; an example is shown in figure 11.

The trajectories of the particles in the two projections may be parametrised using a function of the form $f_q(z) = a_q z + b_q$. A linear, least-squares fit was performed by minimizing the normalised χ^2 given by:

$$\hat{\chi}_q^2 \equiv \chi_q^2 / \nu_q = \frac{1}{\nu_q} \sum_{i=1}^{N_q} \frac{(q_i - f_q(z_i))^2}{\sigma_i^2} = \frac{1}{\nu_q \sigma_0^2} \sum_{i=1}^{N_q} (q_i - f_q(z_i))^2 = \frac{1}{N_q} \sum_{i=1}^{N_q} (q_i - f_q(z_i))^2 . \tag{3}$$
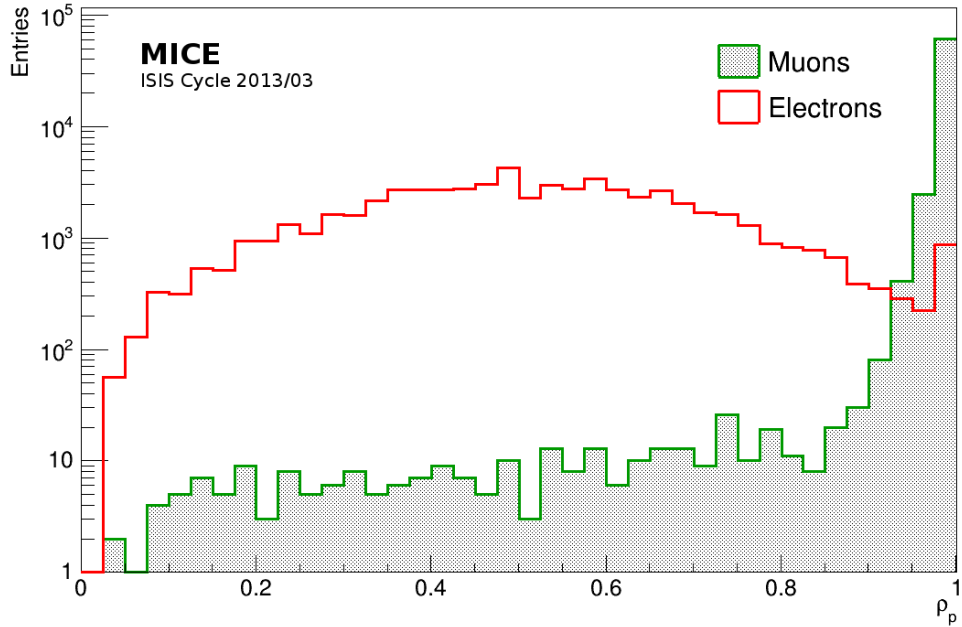
Figure 10: Logarithmic scale distributions of the plane density (ρ_P) for muons and electrons. The integrated electron sample has been normalised to the number of muons.
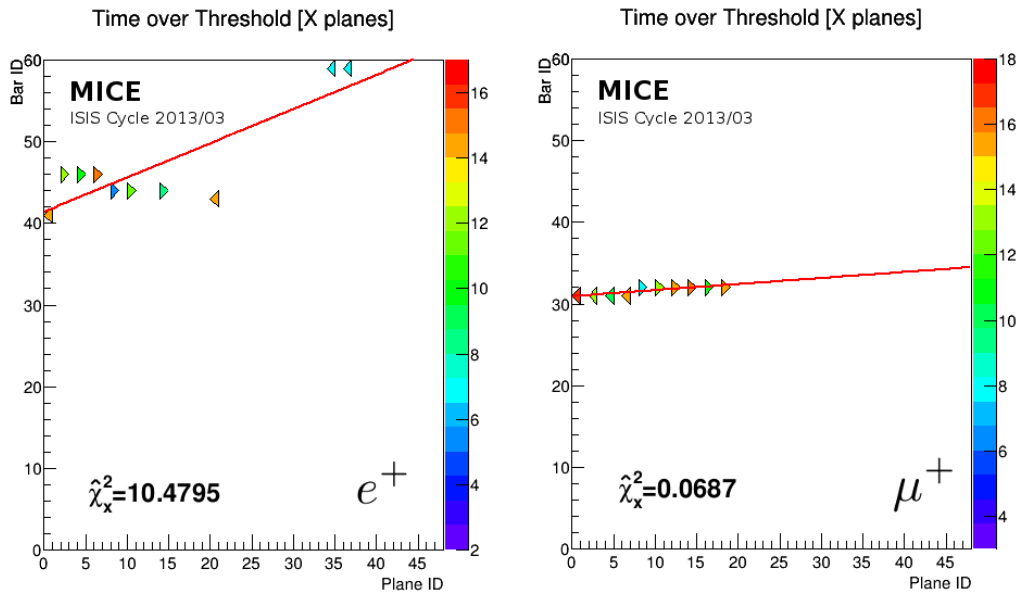

Figure 11: Fitted electron shower and muon track in the xz projection. The location of a hit is defined by the plane number (Plane ID, 0–47) and bar number (Bar ID, 1–59).
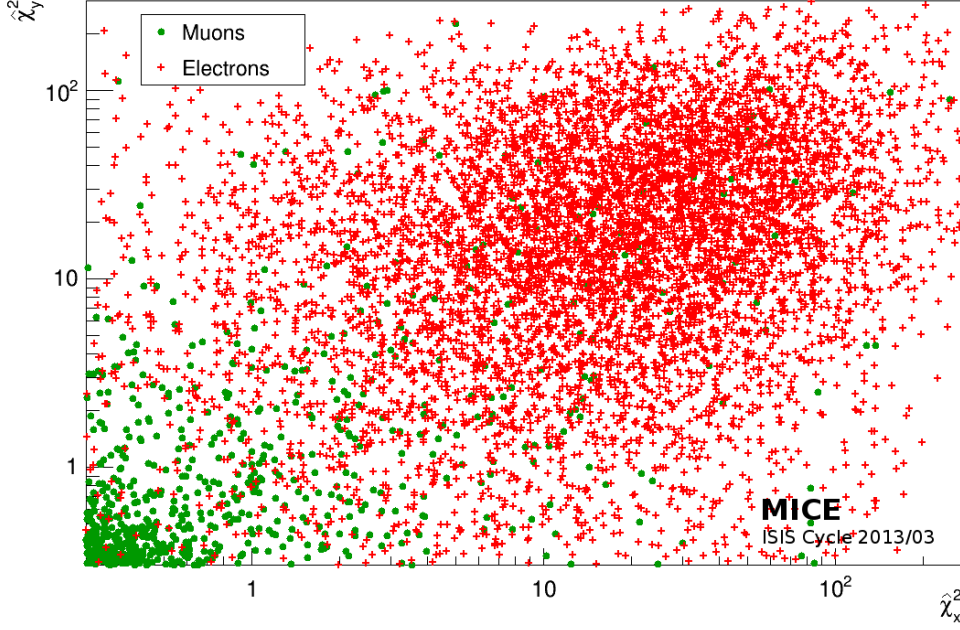
Figure 12: Logarithmic scale scatter plot of the muon and electron samples in the $(\hat{\chi}_x^2, \hat{\chi}_y^2)$ space. $\hat{\chi}_q^2$ is the normalised χ^2 of the linear fit in the qz projection with z along the beam line.

with $\nu_q = \sum_{i=1}^{N_q} \sigma_i^{-2}$, the normalisation constant. As all the points have the same uncertainty (same bar geometry), it is possible to extract the common $\sigma_0^2 \equiv \sigma_i^2$ out of the sum which simplifies the development. Given this definition, it can be shown that the values of a_q and b_q that minimize the normalised χ^2 require that:

- The barycentre $(\langle z \rangle, \langle q \rangle)$ of the points belongs to the polynomial, i.e $\langle q \rangle = a_q \langle z \rangle + b_q$; and
- $a_q = V_{zq}/V_z$ where V_{zq} is the covariance of z and q and V_z is the variance of z.

Under these conditions, the normalised χ^2 in each projection is:

$$\hat{\chi}_q^2 = \sigma_q^2 \left(1 - \mathrm{corr}^2(z, q)\right) ; \tag{4}$$

with $\mathrm{corr}(z, q) = V_{zq}/\sigma_z \sigma_q$ and $\sigma_{z,q}$ the standard deviation of the z and q coordinates respectively. The normalised χ^2 is proportional to σ_q^2, i.e the variance of the q coordinate, which means that the normalised χ^2 increases with the lateral spread of the event in q.

In figure 12, $\hat{\chi}_y^2$ is plotted against $\hat{\chi}_x^2$ for particles identified as electrons and muons. As expected from the definition of these quantities, the majority of the muon sample has a small χ^2 in each of the two projections and is located close to the origin. For electrons, the distribution populates the region of large $\hat{\chi}_x^2$ and $\hat{\chi}_y^2$.

4 Electron-Muon separation

The two variables defined in sections 3.1 and 3.2 were used to develop a general test statistic, T, by which to distinguish muons from electrons. Given an unknown particle P, boundaries, T_C, were defined on these variables such that the null hypothesis H_0 ("is a muon") or the alternative hypothesis H_1 ("is an electron") can be tested.

Two parameters were defined to allow for the hypotheses H_0 and H_1 to be tested. The loss, α, is defined as the proportion of real muons that test negative to H_0, i.e. an error of the first kind or false negatives. The contamination, β, is defined as the proportion of real electrons that test positive to H_0, i.e. an error of the
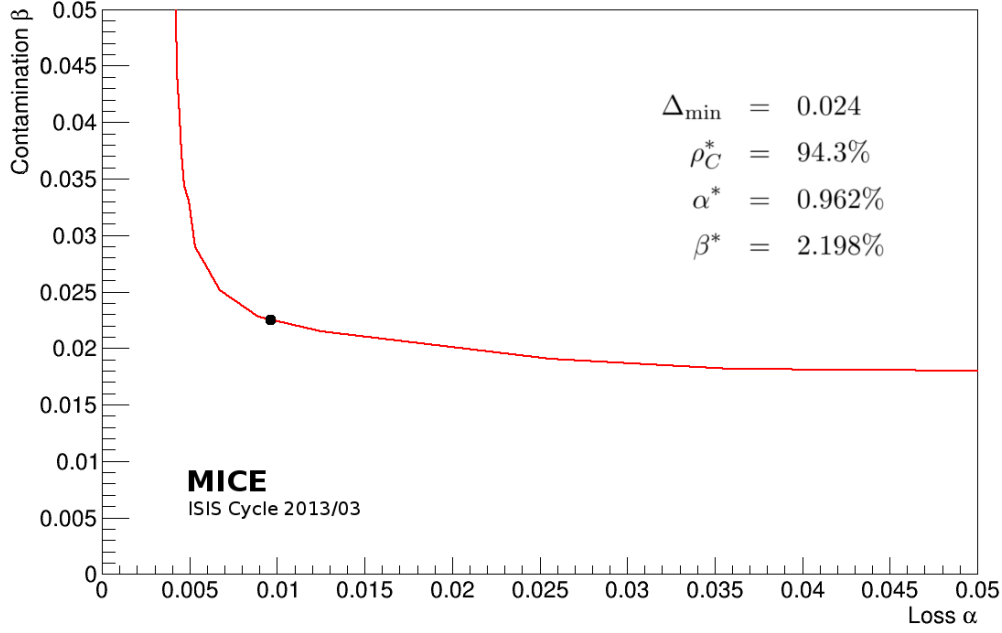
Figure 13: Percentage of the electron sample tagged as a muon (β) as a function of the loss of real muons (α) for different values on the cut ρ_C. The black dot represents the optimal point of the curve.

second kind or false positives. In this context, the most relevant space to work in is the (α, β) space. A test is said to be uniformly more efficient if it has a smaller contamination for any given loss [23].

When the choice of test has been made, a value of the optimal cut, T_C^*, has to be calculated. The optimal value must be such that the corresponding point (α^*, β^*) in the (α, β) space is as close to the origin as possible. Consider the quantity $\Delta = \sqrt{\alpha^2 + \beta^2}$ as the distance between a point of this space to its origin. The value of the cut with the smallest distance $\Delta_{\min}$ is the optimal cut. A perfect test would achieve $\alpha^* = \beta^* = 0$, i.e. no overlap between the two samples.

4.1 Plane density test

Muons tend to have a much higher plane density than their decay products. Given an unknown particle type P, define a cut, ρ_C, such that:

$$\rho_P > \rho_C \rightarrow H_0 \,; \text{ or } \rho_P \leq \rho_C \rightarrow H_1 \,.$$

The particle is tagged as a muon if its plane density is greater than ρ_C and as an electron otherwise. The muon and electron samples are reprocessed for a wide array of cuts and the values of the contamination and the loss are computed for each of them. The results of this scanning are represented in figure 13 in the (α, β) space. The points occupy a single curve in this space because they are the result of a one dimensional cut. The curve is monotonic as raising the cut increases the loss while reducing the contamination.

The distance, Δ, is calculated for each point and the optimum cut is determined. With this single-variable cut, more than 99% of the entire muon sample is identified correctly and the electron contamination is ~2.2% in the muon sample.
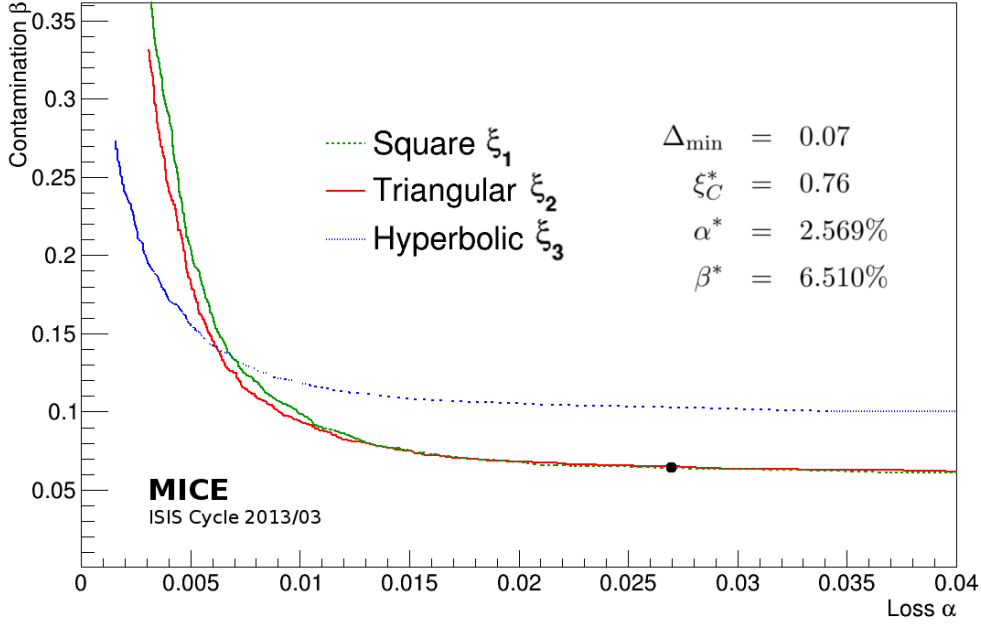
11

Figure 14: Percentage of the electron sample tagged as a muon (β) as a function of the loss of real muons (α) for three choices of test statistic ξ. The black dot is the optimal point regardless of the choice of test statistic.

4.2 Spread test

The shower spread is summarised by two separate values for the two projections $\hat{\chi}_x^2$ and $\hat{\chi}_y^2$. The second test statistic, ξ, is a combination of these two values. The following tests were considered in this analysis:

1. $\xi_1 = \max_{q=x,y} \hat{\chi}_q^2$; largest of the $\hat{\chi}_q^2$. A cut on ξ_1 limits a square area in the $(\hat{\chi}_x^2, \hat{\chi}_y^2)$ space;
2. $\xi_2 = \hat{\chi}_x^2 + \hat{\chi}_y^2$; sum of the $\hat{\chi}_q^2$. A cut on ξ_2 limits a triangular area in the $(\hat{\chi}_x^2, \hat{\chi}_y^2)$ space;
3. $\xi_3 = \hat{\chi}_x^2 \times \hat{\chi}_y^2$; product of the $\hat{\chi}_q^2$. A cut on ξ_3 limits a hyperbolic area in the $(\hat{\chi}_x^2, \hat{\chi}_y^2)$ space.

A study of the electron contamination, β, as a function of the muon loss, α, was performed to determine the best choice for ξ. The results of this analysis are shown in figure 14. For losses below $\sim 0.5\%$, the hyperbolic combination is the most efficient test, but the triangular test yields the lowest contamination for losses above $\sim 0.5\%$ and globally gives the best optimal cut. The square cut produces results similar to the triangular one, but is poorer for low-loss values. Therefore, $\xi \equiv \xi_2 = \hat{\chi}_x^2 + \hat{\chi}_y^2$ was chosen as the test statistic.

Muons produce very low χ^2 straight tracks in the EMR while electrons, that shower in KL, yield much higher values of χ^2. Given an unknown particle P, define a cut, ξ_C, such that:

$$\xi < \xi_C \rightarrow H_0 \,;\, \text{or } \xi \geq \xi_C \rightarrow H_1 \,.$$

The particle is tagged as a muon if ξ is below a certain threshold and as an electron otherwise. A scan for different ξ_C produces the data in figure 14 in the (α, β) space. Once again, for a given choice of test, the points occupy a single dimension and produce a monotonic curve, when the cut is raised the loss decreases and the contamination grows.

The optimal point is obtained by minimizing the distance Δ. The spread test is not as efficient as the density test as both the loss and the contamination are greater. Approximately 97.4% of the muon sample is identified correctly while the electron contamination of the final sample is $\sim 6.5\%$. While not optimal in isolation, the spread test can be used in addition to the density test.
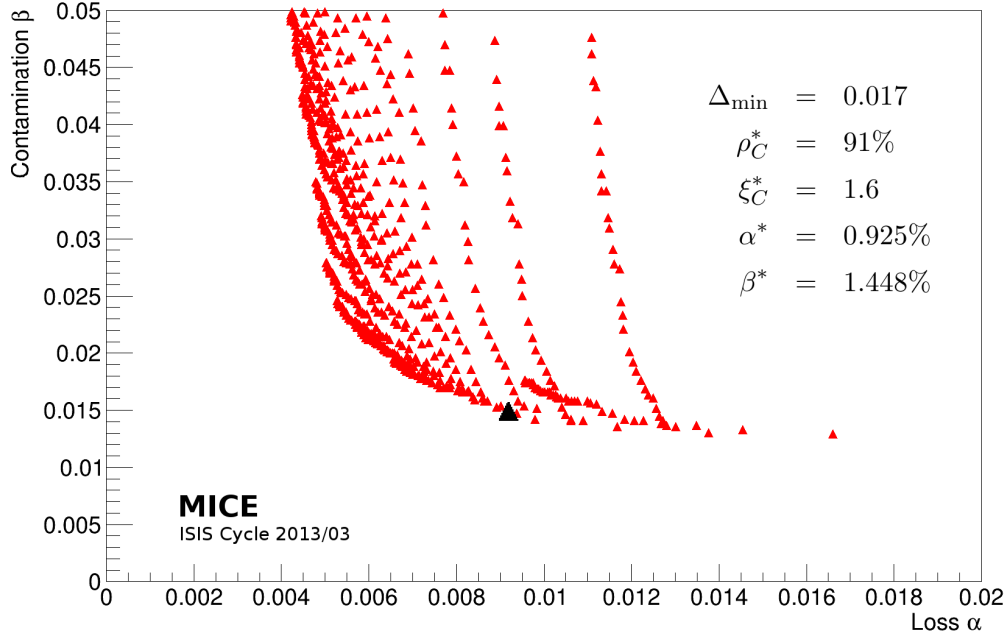
Figure 15: Percentage of the electron sample tagged as a muon (β) versus the loss of real muons (α) in the multivariate analysis. The large black triangle is the optimal point.

4.3 Multivariate test

Combining the two test statistics ρ_P and ξ yields better results than either statistic alone. Given an unknown particle species, consider a set of cuts ρ_C, ξ_C such that:

$$\rho_P > \rho_C \cap \xi < \xi_C \quad \rightarrow \quad H_0 \, ; \text{ or}$$
$$\rho_P \leq \rho_C \cup \xi \geq \xi_C \quad \rightarrow \quad H_1. \tag{5}$$

This is a straightforward combination of the two single-variable tests and represents a triangular prism in the $(\rho_P, \hat{\chi}_x^2, \hat{\chi}_y^2)$ space. It has the advantage of including both features of each particle type into one single test. Muon events that are both dense and narrow will be tagged H_0 while non-continuous and wide electron events will not.

A scan of both cuts produces the plot in figure 15. The points do not form a single monotonic function in the (α, β) space, showing that the two variables ρ_P and ξ are not entirely correlated, i.e. that their combination carries more information than either one alone. For a given ρ_C, the contamination increases with ξ_C.

The most critical element of this electron-muon-separation analysis was to determine the optimal point of this multivariate test, as it provides the best separation efficiency by combining single-variable tests. The optimum choice of cuts indicated in figure 15 yields a muon loss of $\sim 0.9\%$ and an electron contamination of below 1.45%. Both figures are lower than the single-variable tests and hence the multivariate analysis is superior to either single-variable analysis.

For instance, in case of equal abundance of muons and electrons, the EMR will deliver a muon-sample purity of 98.55% with a loss below 1%. Taking all the beam settings combined, the abundance ratio of electrons to muons was 11.7%, producing a purity greater than 99.8% in the final muon sample. In the muon-dominated beam used to demonstrate ionization cooling, the purity provided by the EMR will be much greater than the 99% required by MICE [18].
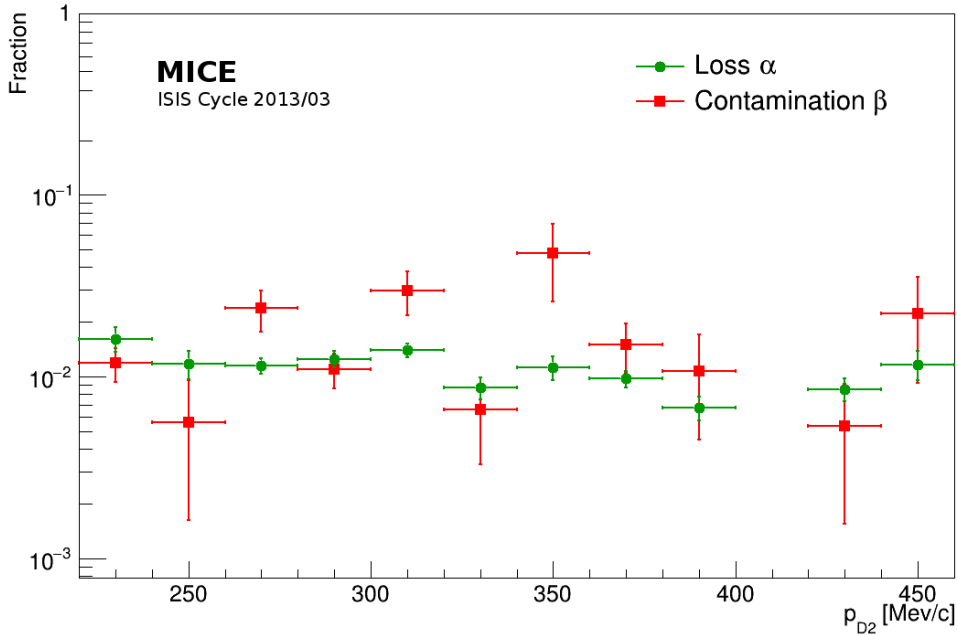
13

Figure 16: Percentage of electron contamination and muon loss for different ranges of momentum set at D2 (p_{D2}). The error bars are based on the statistical uncertainty in a bin.

4.4 Momentum dependence

The previous sections show that the detector functions as designed and reaches the desired efficiency for samples of muons and electrons. It is necessary to check that the multivariate test developed in this analysis is consistently powerful for all momenta set at D2.

The optimal cuts, $\rho_C^* = 0.91$ and $\xi_C^* = 1.6$, were applied for different ranges of momentum and the level of contamination and loss was determined for each range. The loss, α, in figure 16 is $\sim 1\%$ for the full momentum range. The contamination, β, fluctuates around 2%.

5 Muon momentum reconstruction

In its cooling demonstration, MICE will measure the phase-space reduction of a muon beam traversing the cooling cell. This muon beam is selected upstream of the cooling cell by two dipoles in such a way that a beam with very high muon purity enters the experiment [13]. The two trackers measure the muon momentum with great accuracy upstream and downstream of the absorber, provided that the muon has a sufficient transverse momentum, p_T. It is not important for the EMR to be able to measure the pion momentum or that of the rejected electrons. It is interesting, however, to estimate how well the EMR can reconstruct the muon momentum. The EMR can assist the trackers with low p_T muon tracks and can provide a redundant measurement for larger p_T.

5.1 Range reconstruction

In order to avoid problems induced by MAPMT crosstalk, the most energetic hit in each plane, selected in the same way as was done for the estimation of the spread, was used for the range reconstruction.
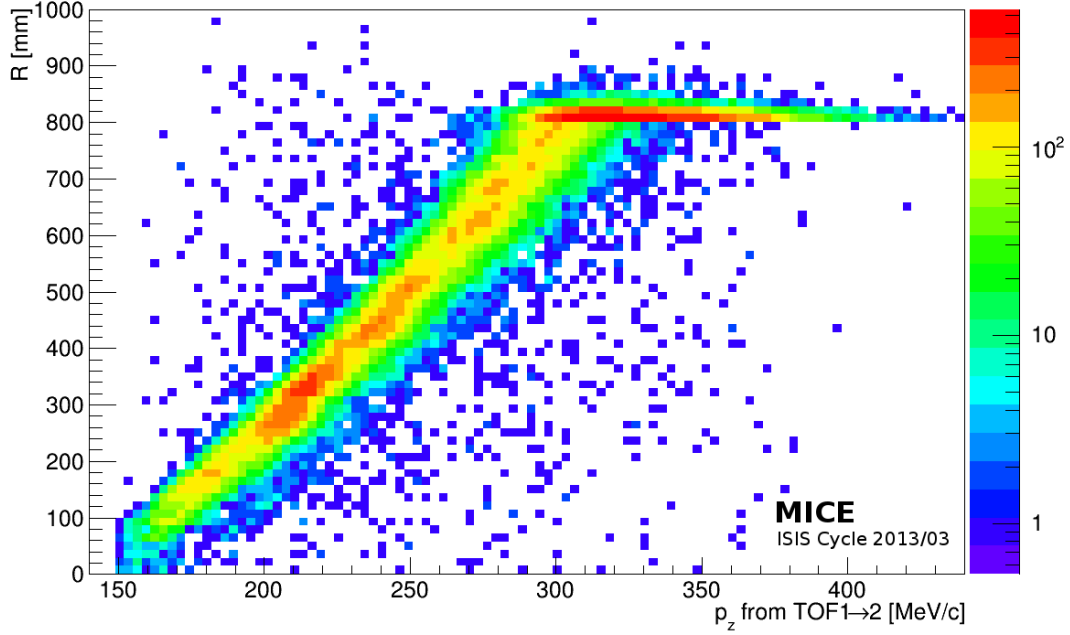
Figure 17: Muon range as a function of the momentum reconstructed from TOF1→2. At 280 MeV/c and above, muons can traverse the entire detector without stopping, hence the plateau at $R \sim 816$ mm.

The reconstruction method uses the linear fit defined in section 3.2. The muon track was fitted in its two separate projections and the pitch of its trajectory was measured in each of them. The angles in the xz and yz projections are θ_x and θ_y, respectively. Provided that the last bar hit by the track has the coordinates (x_N, y_N, z_N), the total range is:

$$R = z_N \sqrt{1 + (\tan^2 \theta_x + \tan^2 \theta_y)} \equiv z_N / \cos \theta \, ; \tag{6}$$

with $\theta = \tan^{-1}\left(\sqrt{\tan^2 \theta_x + \tan^2 \theta_y}\right)$, the total angle with respect to the z axis. The results are shown for the entire muon sample in figure 17.

5.2 Theoretical approximation

In order to give an estimate of the muon momentum from a single range measurement it is necessary to develop a theoretical understanding of the dependence of range on momentum. A fit of the data recorded is used to provide a single estimate of the muon momentum downstream of the cooling channel, p_d, as a function of the range in the EMR. We define an invertible function, f, such that:

$$R = f(p_d) \iff p_d = f^{-1}(R) \, . \tag{7}$$

To construct a manageable function, the EMR geometry is reduced to a simple 816 mm thick block of polystyrene as it is the base material used in the plastic scintillator bars. Finding the range of muons in the EMR is equivalent to computing the range in polystyrene. In this situation, the best approach is the same CSDA method used to calculate the energy loss. For an average muon stopping power, $\langle dE/dx \rangle$, of polystyrene, the CSDA range is:

$$R = \int_{E_0}^{0} \frac{dE}{\langle dE/dx \rangle} = \int_{p_0/m_\mu c}^{0} \frac{dp}{\langle dE/dx \rangle} \beta m_\mu c^2 \, . \tag{8}$$
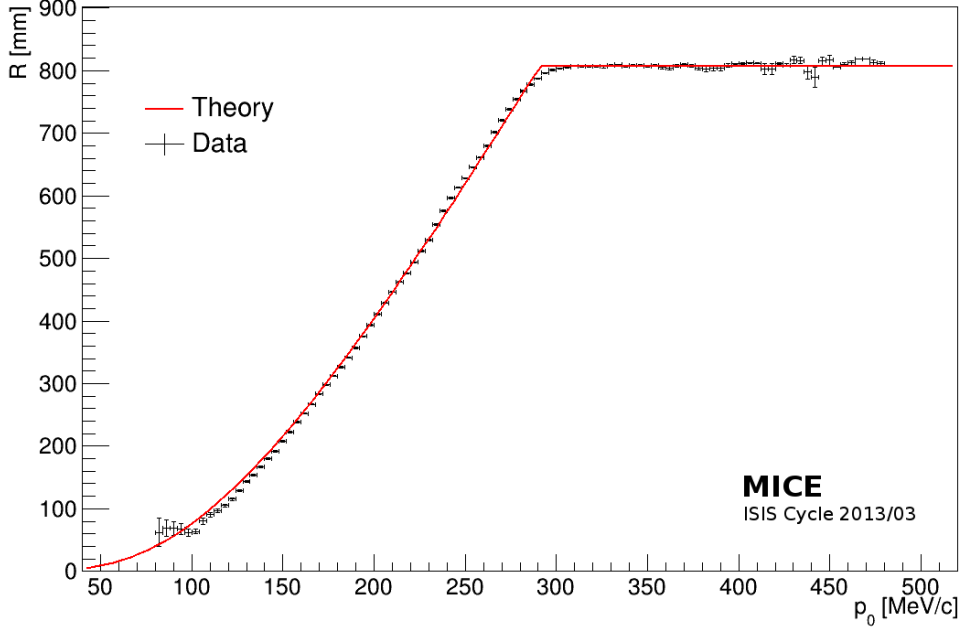
Figure 18: Muon range as a function of the initial momentum $p_0 = p_d - \Delta p(p_d)$. The error bars represent the bin width in abscissa and the uncertainty of the average reconstructed range in ordinate.

The integral in eq. (8) has no analytical solution due to the complexity of the Bethe-Bloch formula. However, it can be integrated numerically for a muon of initial momentum p_0. The function can also be inverted numerically to give an estimate of the momentum.

p_d is the momentum of the muon just before it enters TOF2 and corresponds to the momentum reconstructed from TOF1→2. This constitutes a complication because it is significantly different from the initial momentum in the EMR, p_0. The function f^{-1} provides an estimate of the range for a given p_0, but must compensate for the combined momentum loss in TOF2 and KL, $\Delta p(p_d)$. The correction, $p_0 = p_d - \Delta p(p_d)$, has to be applied muon by muon.

Figure 18 shows the range of muons in the EMR as a function of their initial momentum, p_0. The CSDA prediction shows very good agreement with data for $p_0 > 150 \, \mathrm{MeV}/c$ while the agreement is acceptable for lower p_0 (the plateau of the simulation is added to fit the dimensions of the EMR). The agreement could be improved by a more detailed analysis of the KL, this is beyond the scope of this paper. However, the approximation presented here is a powerful tool that allows an estimate of momentum to be made.

5.3 Momentum reconstruction accuracy

Provided with an estimation of the initial momentum, p_0, the uncertainty on the unfolding of p_d may be estimated. There are several sources of uncertainty:

- The uncertainty on the time of flight $\sigma_t \sim 70 \, \mathrm{ps}$ and path length $\sigma_s \sim 1 \, \mathrm{cm}$;
- Fluctuation of the momentum-loss in KL as a function of p_d;
- The uncertainty on the longitudinal position in the EMR, $\sigma_z \sim 5 \, \mathrm{mm}$.

Figure 19 shows that the RMS of the momentum distribution in a given plane in the centre of the detector is $\sim 10 \, \mathrm{MeV}/c$. Each bin represents a single plane of the EMR (17 mm in depth). At the entrance of the fiducial volume, muons of low momentum stop in the first few planes and the RMS is large. At the back of the detector,
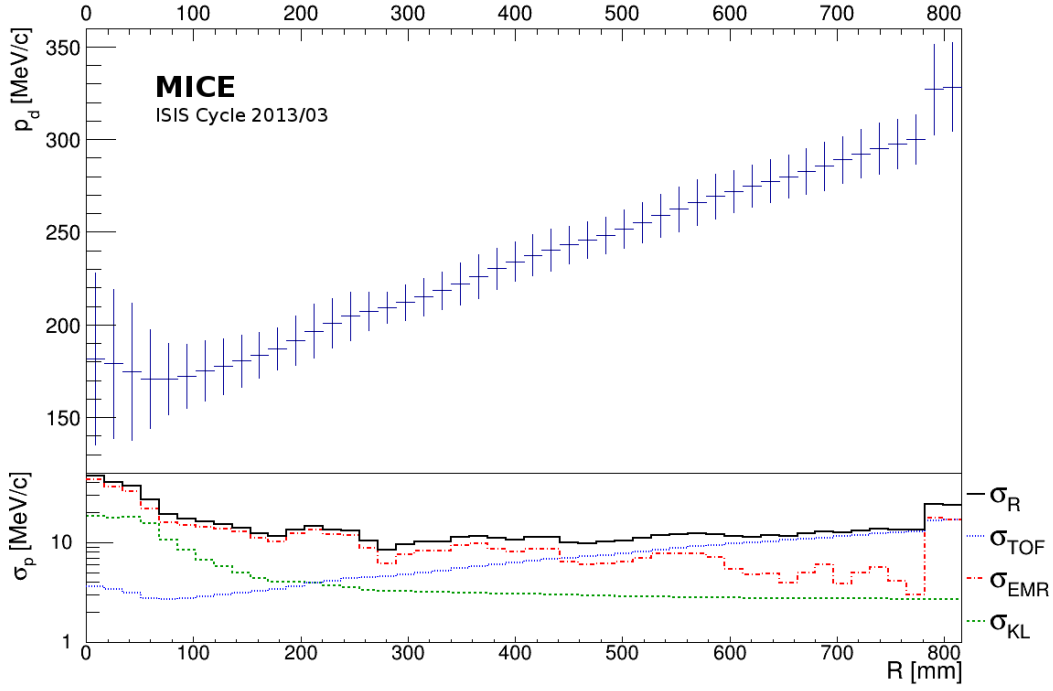
16

Figure 19: Downstream momentum (p_d) as a function of the range (R) in the EMR. A bin corresponds to a plane and its error bar represents the RMS of the momentum distribution within the bin.

the muons with momentum above $320\,\mathrm{MeV}/c$ cross the entire detector and thus the last two planes are biased towards higher values.

The uncertainty on p_d emerging from the TOF momentum reconstruction, with t the time-of-flight measurement, can be shown to be:

$$\sigma_\mathrm{TOF} = \frac{m_\mu c^2 t}{s^2}\left(\left(\frac{ct}{s}\right)^2 - 1\right)^{-3/2}\sigma_t \oplus \frac{m_\mu c^2 t^2}{s^3}\left(\left(\frac{ct}{s}\right)^2 - 1\right)^{-3/2}\sigma_s\,, \tag{9}$$

with $\oplus$ indicating the quadratic sum. σ_TOF ranges from 3–$15\,\mathrm{MeV}/c$ for momenta from 150–$350\,\mathrm{MeV}/c$. As a bin contains a range of momenta, eq. (9) is averaged over a normal p.d.f. centred on the average momentum in the bin and with a width equal to the bin RMS in order to produce σ_TOF.

The spread of the energy loss in KL is computed using the distribution of momentum loss, $f_p(\Delta p)$, given for an array of momenta, p, as shown in figure 7. A single momentum-loss distribution, $f_i(\Delta p)$, constructed for a bin centred in R_i, is defined as:

$$f_i(\Delta p) = \int_0^{+\infty} f_p(\Delta p)\frac{1}{\sqrt{\pi}\sigma_i}e^{-\frac{(p-p_i)^2}{\sigma_i^2}}\,\mathrm{d}p\,; \tag{10}$$

with $1/(\sqrt{\pi}\sigma_i)e^{-\frac{(p-p_i)^2}{\sigma_i^2}}$ the normal distribution centred on the average momentum in the bin, p_i, and with width equal to the bin RMS, σ_i. The RMS of $f_i(\Delta p)$ is used as the uncertainty on the momentum from the momentum loss in KL, σ_KL.

The total uncertainty on the momentum from the range measurement, R_μ, can be summarized as:

$$\sigma_R = \sigma_\mathrm{TOF} \oplus \sigma_\mathrm{KL} \oplus \sigma_\mathrm{EMR}\,; \tag{11}$$

and therefore, given that the uncertainties are not correlated:

$$\sigma_\mathrm{EMR} \sim \sqrt{\sigma_R^2 - \sigma_\mathrm{TOF}^2 - \sigma_\mathrm{KL}^2}\,; \tag{12}$$

17

Figure 19 shows a compilation of the uncertainties originating from the different components of this analysis. For small values of the range, the EMR has a poor resolution and does not produce reliable momentum reconstruction. After about 10 planes, the total spread reaches its nominal value of $\sim 10\,\mathrm{MeV}/c$ and is constant until the last two planes where the values are biased by the muons exiting the detector. The EMR itself, subtracting the errors from KL and TOF, achieves resolutions down to $3\,\mathrm{MeV}/c$ for larger range.

6   Conclusions

The ability of the Electron-Muon Ranger (EMR) to separate electrons from muons has been demonstrated. It is known from simulation [24] that muons and electrons produce distinct signal patterns: muons below a certain energy stop in the detector and the energy deposition exhibits a clear Bragg peak, the position of which defines the range. Electrons shower in KL and exhibit multiple tracks in the EMR. In order to verify this, the EMR was exposed to a beam containing both types of particles with momenta in the range 100–400 MeV/c. As expected, electrons and muons produce substantially different patterns so that electrons can be identified with 98.6% efficiency using the EMR alone.

The detector was not tuned or optimized prior to the measurements. Nevertheless, the detector was able to separate electrons from muons using a simple test statistic on two variables based on the transverse and longitudinal structure of an event.

The detector provides tracking and calorimetric information. Tracks and showers can be reconstructed and identified as muons or electrons. A Bragg peak at the end of muon and pion tracks marks the place where a particle stops and, therefore, helps in measuring the range. It was shown that the muon range can be used to infer the particle momentum in the Continuously Slowing Down Approximation with very good accuracy.

Acknowledgements

References

[1] **IDS-NF** Collaboration, S. Choubey and *et al.*, "International Design Study for the Neutrino Factory, Interim Design Report," tech. rep., 2011. `arXiv:1112.2853`.

[2] M. Alsharo'a and *et al. Phys. Rev. ST Accel. Beams* **6** (Aug, 2003) 081001.

[3] V. Parkhomchuck and A. Skrinsky, "Cooling Methods for Charged Particle Beams," *Rev.Accel.Sci.Tech.* **1** no. 1, (2008) 237.

[4] **ISS Accelerator Working Group** Collaboration, M. Apollonio and *et al.*, "Accelerator design concept for future neutrino facilities," *Journal of Instrumentation* **4** no. 7, (2009) .

[5] R. Palmer, A. Sessler, A. Skrinsky, A. Tollestrup, A. Baltz, *et al.*, "Muon collider design," *Nucl.Phys.Proc.Suppl.* **51A** (1996) 61–84, `arXiv:acc-phys/9604001 [acc-phys]`.

[6] **MICE** Collaboration, G. Gregoire, G. Ryckewaert, L. Chevalier, J. Rey, M. Catanesi, *et al.*, "Proposal to the Rutherford Appleton Laboratory: an International Muon Ionization Cooling Experiment (MICE),". `http://mice.iit.edu/micenotes/public/pdf/MICE0021/MICE0021.pdf`. MICE-NOTE-21.

[7] D. Neuffer, "Principles and Applications of Muon Cooling," *Part.Accel.* **14** (1983) 75.

[8] D. Neuffer, "Multi-TeV Muon Colliders," *AIP Conf.Proc.* **156** (1987) 201–208.

[9] M. Palmer and *et al.*, "Muon accelerators for the next generation of high energy physics experiments," 13th International Particle Accelerator Conference (IPAC 13), Shanghai, China, 2013.

[10] "Muon ionization cooling experiment,". `http://mice.iit.edu`.

[11] R. Asfandiyarov, "A totally active scintillator calorimeter for the Muon Ionization Cooling Experiment (MICE). Design and construction," *Nucl.Instrum.Meth.* **A732** (2013) 451–456.

[12] R. C. Fernow and R. B. Palmer, "Solenoidal ionization cooling lattices," *Phys. Rev. ST Accel. Beams* **10** (Jun, 2007) 064001.

[13] **MICE** Collaboration, M. Bogomilov and *et al.*, "The MICE Muon Beam on ISIS and the beam-line instrumentation of the Muon Ionization Cooling Experiment," *Journal of Instrumentation* **7** no. 5, (2012) P05009.

[14] **MICE** Collaboration, V. Blackmore, C. Hunt, J. Pasternak, C. Rogers, P. Snopok, and H. Witte, "MICE Ionization Cooling Demonstration: Technical Note,". `http://mice.iit.edu/mnp/MICE0452.pdf`. MICE-NOTE-DET-452.

[15] "Isis pulsed neutron and muon source at the rutherford appleton laboratory,". `http://www.isis.stfc.ac.uk`.

[16] C. N. Booth and *et al.*, "The design, construction and performance of the MICE target," *Journal of Instrumentation* **8** no. 03, (2013) P03006.

[17] R. Bertoni and *et al.*, "The design and commissioning of the MICE upstream time-of-flight system," *Nucl. Inst. Meth. A* **615** no. 1, (2010) 14 – 26.

[18] **MICE** Collaboration, M. Rayner and M. Bonesini, "The MICE PID Detector System," tech. rep., 2010. `http://mice.iit.edu/mnp/MICE0304.pdf`. MICE-NOTE-304.

[19] **MICE** Collaboration, R. Bertoni, A. Bonesini, A. de Bari, G. Cecchet, Y. Karadzhov, and R. Mazza, "The construction of the MICE TOF2 detector,". `http://mice.iit.edu/mnp/MICE0286.pdf`. MICE-NOTE-DET-286.

[20] R. Asfandiyarov, *Totally Active Scintillator Tracker-Calorimeter for the Muon Ionization Cooling Experiment*. PhD thesis, University of Geneva, Jul, 2014. CERN-THESIS-2014-164.

[21] N. Carron, *An Introduction to the Passage of Energetic Particles through Matter*. Taylor & Francis, 2006. `https://books.google.co.uk/books?id=LRAHeoBP_l8C`.

[22] **MICE** Collaboration, R. Asfandiyarov, A. Blondel, and F. Drielsma, "Crosstalk and Misalignment in the Electron Muon Ranger (EMR),". `http://mice.iit.edu/mnp/MICE0440.pdf`. MICE-NOTE-DET-440.

[23] F. James, *Statistical Methods in Experimental Physics*. World Scientific Publishing, 2006. `https://books.google.co.uk/books?id=S8N_QgAACAAJ`.

[24] **MICE** Collaboration, R. Asfandiyarov, A. Blondel, and L. Haegel, "Geant4 Simulation of the EMR Detector Response Study,". `http://mice.iit.edu/mnp/MICE0388.pdf`. MICE-NOTE-DET-388.

The MICE collaboration

M. Bogomilov, R. Tsenov, G. Vankova-Kirilova
Department of Atomic Physics, St. Kliment Ohridski University of Sofia, Sofia, Bulgaria

R. Bertoni, M. Bonesini, F. Chignoli, R. Mazza
Sezione INFN Milano Bicocca, Dipartimento di Fisica G. Occhialini, Milano, Italy

V. Palladino
Sezione INFN Napoli and Dipartimento di Fisica, Università Federico II, Complesso Universitario di Monte S. Angelo, Napoli, Italy

A. de Bari, G. Cecchet
Sezione INFN Pavia and Dipartimento di Fisica, Pavia, Italy

M. Capponi, A. Iaciofano, D. Orestano, F. Pastore[a], L. Tortora
Sezione INFN Roma Tre e Dipartimento di Fisica, Roma, Italy

Y. Kuno, H. Sakamoto
Osaka University, Graduate School of Science, Department of Physics, Toyonaka, Osaka, Japan

S. Ishimoto
High Energy Accelerator Research Organization (KEK), Institute of Particle and Nuclear Studies, Tsukuba, Ibaraki, Japan

F. Filthaut[b]
Nikhef, Amsterdam, The Netherlands

O. M. Hansen, S. Ramberger, M. Vretenar
CERN, Geneva, Switzerland

R. Asfandiyarov, P. Bene, A. Blondel, F. Cadoux, S. Debieux, F. Drielsma[*], J. S. Graulich, C. Husi, Y. Karadzhov, F. Masciocchi, L. Nicola, E. Noah Messomo, K. Rothenfusser, R.Sandström, H. Wisting
DPNC, Section de Physique, Université de Genève, Geneva, Switzerland

G. Charnley, N. Collomb, A. Gallagher, A. Grant, S. Griffiths, T. Hartnett, B. Martlew, A. Moss, A. Muir, I. Mullacrane, A. Oates, P. Owens, G. Stokes, P. Warburton, C. White
STFC Daresbury Laboratory, Daresbury, Cheshire, UK

D. Adams, P. Barclay, V. Bayliss, T. W. Bradshaw, M. Courthold, V. Francis, L. Fry, T. Hayler, M. Hills, A. Lintern, C. Macwaters, A. Nichols, R. Preece, S. Ricciardi, C. Rogers, T. Stanley, J. Tarrant, S. Watson, A. Wilson
STFC Rutherford Appleton Laboratory, Harwell Oxford, Didcot, UK

---

[a]Deceased

[b]Also at Radboud University, Nijmegen, The Netherlands

[*]Corresponding author.

R. Bayes, J. C. Nugent, F. J. P. Soler
School of Physics and Astronomy, Kelvin Building, The University of Glasgow, Glasgow, UK

P. Cooke, R. Gamet
Department of Physics, University of Liverpool, Liverpool, UK

A. Alekou, M. Apollonio, G. Barber, D. Colling, A. Dobbs, P. Dornan, C. Hunt, J-B. Lagrange, K. Long, J. Martyniak, S. Middleton, J. Pasternak, E. Santos, T. Savidge, M. A. Uchida
Department of Physics, Blackett Laboratory, Imperial College London, London, UK

V. J. Blackmore[c],T. Carlisle, J. H. Cobb, W. Lau, M. A. Rayner, C. D. Tunnell
Department of Physics, University of Oxford, Denys Wilkinson Building, Oxford, UK

C. N. Booth, P. Hodgson, J. Langlands, R. Nicholson, E. Overton, M. Robinson, P. J. Smith
Department of Physics and Astronomy, University of Sheffield, Sheffield, UK

A. Dick, K. Ronald, D. Speirs, C. G. Whyte, A. Young
Department of Physics, University of Strathclyde, Glasgow, UK

S. Boyd, P. Franchini, J. Greis, C. Pidcott, I. Taylor
Department of Physics, University of Warwick, Coventry, UK

R. Gardener, P. Kyberd, M. Littlefield, J. J. Nebrensky
Brunel University, Uxbridge, UK

A. D. Bross, T. Fitzpatrick[a], M. Leonova, A. Moretti, D. Neuffer, M. Popovic, P. Rubinov, R. Rucinski
Fermilab, Batavia, IL, USA

T. J. Roberts
Muons, Inc., Batavia, IL, USA

D. Bowring, A. DeMello, S. Gourlay, D. Li, S. Prestemon, S. Virostek, M. Zisman[a]
Lawrence Berkeley National Laboratory, Berkeley, CA, USA

P. Hanlet, G. Kafka, D. M. Kaplan, D. Rajaram, P. Snopok, Y. Torun
Illinois Institute of Technology, Chicago, IL, USA

S. Blot, Y. K. Kim
Enrico Fermi Institute, University of Chicago, Chicago, IL, USA

U. Bravar
University of New Hampshire, Durham, NH, USA

Y. Onel
Department of Physics and Astronomy, University of Iowa, Iowa City, IA, USA

---

[c]Now at Department of Physics, Blackett Laboratory, Imperial College London, London, UK

L. M. Cremaldi, T. L. Hart, T. Luo, D. A. Sanders, D. J. Summers
University of Mississippi, Oxford, MS, USA

D. Cline[a], X. Yang
University of California, Los Angeles, CA, USA

L. Coney, G. G. Hanson, C. Heidt
University of California, Riverside, CA, USA